Nuclear Science and Techniques (2023) 34:173
https://doi.org/10.1007/s41365-023-01316-x

# Pairing effects on the fragment mass distribution of Th, U, Pu, and Cm isotopes

**Xin Guan**[1] · **Jin-Huan Zheng**[1] · **Mei-Yan Zheng**[1]

Received: 1 July 2023 / Revised: 20 July 2023 / Accepted: 29 July 2023 / Published online: 21 November 2023


**Abstract**

In this article, a comprehensive study of the fission process of Th, U, Pu, and Cm isotopes using a Yukawa-folded mean-field plus standard pairing model is presented. The study focused on analyzing the effects of the pairing interaction on the fragment mass distribution and its dependence on nuclear elongation. The significant role of pairing interactions in the fragment mass distributions of $^{230}$Th, $^{234}$U, $^{240}$Pu, and $^{246}$Cm was demonstrated. Numerical analysis revealed that increasing the pairing interaction strength decreased the asymmetric fragment mass distribution and increased the symmetric distribution. Furthermore, the odd-even mass differences at symmetric and asymmetric fission points were examined, highlighting their sensitivity to changes in the pairing interaction strength. Systematic analysis of the Th, U, Pu, and Cm isotope fragment mass distributions demonstrated the effectiveness of the model in reproducing the experimental data. In addition, the effects of the zero-point energy and half-width parameter on the fragment mass distribution for $^{240}$Pu were explored. Thus, this study provides valuable insights into the fission process by emphasizing the importance of pairing interactions and their relationship with nuclear elongation.

**Keywords** Nuclear fission · Pairing interaction · Fragment mass distribution · Actinide nuclei

## 1 Introduction

Nuclear fission is a fundamental process that plays a key role in modern nuclear technology. The theoretical calculation of the fission process is a complex and challenging problem, which necessitates the utilization of advanced nuclear models and computational techniques [1–6]. Over the years, numerous theoretical models, ranging from simple empirical models to sophisticated microscopic models based on the nuclear structure and reaction theory, have been developed to predict fission yields [7–9]. These models, which have been validated against experimental data, have proven to be valuable tools for predicting the behavior of nuclear systems.

This work was supported by the National Natural Science Foundation of China (Nos. 12275115 and 12175097) and the Educational Department of Liaoning Province (No. LJKMZ20221410).

✉ Xin Guan
guanxin@lnnu.edu.cn

1 Department of Physics, Liaoning Normal University, Dalian 116029, China

Pairing interactions significantly affect the properties of the fissioning nucleus and resulting fission products [10–15]. For instance, the strength of the pairing interaction strongly influences the shapes of the barriers that separate the ground state from scission [16–20], fission fragment distributions [21–25], and spontaneous fission lifetimes [26]. In the dynamic description of nuclear fission, pairing interactions should be considered on the same footing as those associated with the shape degrees of freedom [15]. Understanding the role of pairing interactions in nuclear fission is being actively researched, and various theoretical models have been developed to describe their behavior in different fission scenarios. Macroscopic-microscopic studies have demonstrated that pairing fluctuations can significantly reduce collective action and affect the predicted spontaneous fission lifetimes [27]. In the Hartree-Fock-Bogoliubov (HFB) model, pairing can be self-consistently included by extending the trial space to quasi-particle Slater determinants [22, 28]. Theoretical studies based on the HFB method revealed that the effect of pairing interactions hinders collective rotation, reduces level crossings, and shortens the half-life of spontaneous fission [29]. The role of dynamic pairing in induced fission dynamics was investigated using the time-dependent generator coordinate method in the Gaussian overlap approximation based on the microscopic framework of nuclear energy density functionals [30]. The inclusion of dynamic pairing has been shown to significantly affect the collective inertia, flux through the scission hypersurface, and resulting fission yields. The latest research on the fission dynamics mechanism of $^{240}$Pu, which is based on the time-dependent Hartree–Fock (HF) method, demonstrates that as dynamical pairing diminishes at high excitations, the random transitions between single-particle levels around the Fermi surface, that mimic thermal fluctuations, becomes indispensable in driving fission [31].

Recently, an iterative algorithm [32, 33] was employed to investigate the fission barriers and static fission paths of Th, U, and Pu isotopes using a deformed mean-field plus standard pairing model with an exact pairing solution [34]. This innovative approach provided a precise representation of pairing interactions in nuclear fission and avoided artifacts introduced by Bardeen–Cooper–Schrieffer calculations, such as the non-conservation of particle numbers and pairing collapse phenomena [11]. A comprehensive investigation of the inner and outer fission barriers in even-even nuclei of Th, U, and Pu isotopes clearly demonstrated the ability of the standard pairing model to closely replicate the experimental inner and outer barrier heights in comparison with the BCS scheme [34]. Moreover, researchers employed the deformed mean-field plus standard pairing model to explore the influence of pairing interactions on the scission configurations, total kinetic energy, and mass distributions of U isotopes [35]. The model successfully reproduced the total kinetic energy and fragment mass distributions of $^{232-238}$U isotopes, which exhibited excellent agreement with the experimental data. The results highlighted the sensitivity of the scission region to variations in the pairing interaction strength, particularly for asymmetric and symmetric scission points. Notably, changes in the peak-to-valley ratio of the mass distribution resulting from variations in the pairing interaction strength underscored the significant impact of pairing interactions on the fission process of $^{236}$U within this model.

It is of paramount importance to develop reliable and effective models for characterizing the fragment mass distribution. Actinide nuclei play a crucial role in assessing the reliability of these models when studying the fragment mass distribution. Therefore, extending our previous research to describe actinide nuclei and investigating the influence of interactions on fragment mass distribution is not only necessary but also highly meaningful. This research endeavor will enhance our understanding of nuclear fission involving heavy nuclei and improve the accuracy of predictive models.

This study presents a systematic analysis of the fission fragment mass distributions in Th, U, Pu, and Cm isotopes using a deformed mean-field plus standard pairing model. The potential energy was calculated within the macroscopic-microscopic framework, incorporating the Fourier shape parameterization combined with the least significant difference (LSD) model and Yukawa-folded potential. The mass distribution of fission fragments was described using a three-dimensional collective model of the Born–Oppenheimer approximation. Extending on our previous study in Ref. [35], this study provides a comprehensive analysis of the impact of pairing on the mass distribution of fission fragments across Th, U, Pu, and Cm isotope chains.

## 2 Theoretical framework and numerical details

### 2.1 Deformed mean-field plus standard pairing model

The Hamiltonian of the deformed mean-field plus standard pairing model for either the proton or neutron sector is given by

$$\hat{H} = \sum_{i=1}^{n} \epsilon_i \hat{n}_i - G \sum_{ii'} S_i^+ S_{i'}^- . \tag{1}$$

Here, the sums run over all given $i$-double degeneracy levels of the total number $n$, while $G > 0$ represents the overall pairing interaction strength. The single-particle energies $\epsilon i$ are obtained using mean-field methods such as the Yukawa-folded single-particle potential, Woods-Saxon potential, and HF. The fermion number operator for the $i$-th double degeneracy level is defined as $n_i = a_{i\uparrow}^\dagger a_{i\uparrow} + a_{i\downarrow}^\dagger a_{i\downarrow}$, and the pair creation (annihilation) operator is represented by $S_i^+ = a_{i\uparrow}^\dagger a_{i\downarrow}^\dagger$ $[S_i^- = (S_i^+)^\dagger = a_{i\downarrow} a_{i\uparrow}]$. The up and down arrows in these expressions refer to time-reversed states.

Using the Richardson–Gaudin method [36–41], the exact $k$-pair eigenstates of (1) with $\nu_{i'} = 0$ for even systems and $\nu_{i'} = 1$ for odd systems, where $i'$ labels the double degeneracy level occupied by an unpaired single particle, can be expressed as

$$|k;\xi;\nu_{i'}\rangle = S^+(x_1^{(\xi)}) S^+(x_2^{(\xi)}) \cdots S^+(x_k^{(\xi)}) |\nu_{i'}\rangle. \tag{2}$$

Here, $|\nu_{i'}\rangle$ is the pairing vacuum state with seniority $\nu_{i'}$ satisfying $S_i^- |\nu_{i'}\rangle = 0$ and $\hat{n}_i |\nu_{i'}\rangle = \delta_{i'} \nu_i |\nu_{i'}\rangle$ for all $i$. $\xi$ is an additional quantum number for distinguishing between different eigenvectors with the same quantum number $k$ and

$$S^+(x_\mu^{(\xi)}) = \sum_{i=1}^{n} \frac{1}{x_\mu^{(\xi)} - 2\epsilon_i} S_i^+ , \tag{3}$$

where the spectral parameters $x_\mu^{(\xi)}$ $(\mu = 1, 2, \ldots, k)$ satisfy the following set of Bethe ansatz equations:

$$1 + G\sum_i \frac{\Omega_i}{x_\mu^{(\xi)} - 2\varepsilon_i} - 2G\sum_{\mu'=1(\neq\mu)}^{k} \frac{1}{x_\mu^{(\xi)} - x_{\mu'}^{(\xi)}} = 0. \tag{4}$$

Here, the first sum runs over all $i$ levels and $\Omega_i = 1 - \delta_{ii'}\nu_{i'}$. For each solution, the corresponding eigenenergy is given by:

$$E_k^{(\xi)} = \sum_{\mu=1}^{k} x_\mu^{(\xi)} + \nu_{i'}\varepsilon_{i'}. \tag{5}$$

The general method for obtaining solutions of Eq. (4) is based on the polynomial approach described in Refs. [42–45]. This approach involves solving the second-order Fuchsian equation [46], given by

$$A(x)P''(x) + B(x)P'(x) - V(x)P(x) = 0, \tag{6}$$

where $A(x) = \prod_{i=1}^{n}(x_\mu^{(\xi)} - 2\varepsilon_i)$ is an $n$-degree polynomial

$$B(x)/A(x) = -\sum_{i=1}^{n} \frac{\Omega_i}{x_\mu^{(\xi)} - 2\varepsilon_i} - \frac{1}{G}. \tag{7}$$

The polynomials $V(x)$, also known as Van Vleck polynomials [46], are of degree $n - 1$ and are determined based on Eq. (6). They are defined as follows:

$$V(x) = \sum_{i=0}^{n-1} b_i x^i. \tag{8}$$

The polynomials $P(x)$ with zeros corresponding to the solutions of Eq. (4) are defined as

$$P(x) = \prod_{i=1}^{k}(x - x_i^{(\xi)}) = \sum_{i=0}^{k} a_i x^i. \tag{9}$$

Here, $k$ represents the number of pairs, while $b_i$ and $a_i$ are the expansion coefficients that must be determined instead of the Richardson variables $x_i$. Additionally, when we set $a_k = 1$ in $P(x)$, the coefficient $a_{k-1}$ is equal to the negative sum of the $P(x)$ zeros, that is, $a_{k-1} = -\sum_{i=1}^{k} x_i^{(\xi)} = -E_k^{(\xi)}$.

For doubly degenerate systems with $\Omega_i = 1$, if the value of $x$ approaches twice the single-particle energy of a given level $\delta$, that is, $x = 2\varepsilon_\delta$, Eq. (6) can be rewritten as follows [42, 45]:

$$\left(\frac{P'(2\varepsilon_\delta)}{P(2\varepsilon_\delta)}\right)^2 - \frac{1}{G}\left(\frac{P'(2\varepsilon_\delta)}{P(2\varepsilon_\delta)}\right) = \sum_{i\neq\delta} \frac{\left[\left(\frac{P'(2\varepsilon_\delta)}{P(2\varepsilon_\delta)}\right) - \left(\frac{P'(2\varepsilon_i)}{P(2\varepsilon_i)}\right)\right]}{2\varepsilon_\delta - 2\varepsilon_i}. \tag{10}$$

An iterative algorithm for obtaining the exact solution of the standard pairing problem using the Richardson-Gaudin method was established by employing the polynomial approach described in Eq. (10) [32]. This algorithm is remarkably efficient and robust and can handle both spherical and deformed systems on a large scale. A crucial element that contributes to its success is the determination of initial estimates for large-set nonlinear equations, ensuring control and adherence to fundamental physical principles. Moreover, the algorithm effectively addresses the challenges of nonsolutions and numerical instabilities that are frequently encountered in existing approaches by reducing the high-dimensional problem to a one-dimensional Monte Carlo sampling procedure. By leveraging this innovative iterative algorithm, we employed the model to explore actinide nuclei isotopes and obtained remarkable agreement with experimental data [32–35].

## 2.2 Fourier shape parameterization

Recent studies have highlighted the remarkable efficiency of Fourier parameterization in describing the essential features of deformed nuclear shapes, extending up to the scission configuration [7, 47]. Based on these findings, the present work employs the innovative Fourier parameterization of nuclear shapes in conjunction with the LSD and Yukawa-folded macroscopic-microscopic potential-energy prescription, and obtains highly efficient results [35, 48, 49]. In particular, the macroscopic-microscopic framework introduced in Ref. [35] served as the foundation for this study. In this framework, the single-particle energies $\varepsilon_i$ in the model Hamiltonian (1) were derived from the Yukawa-folded potential. The expansion of the nuclear surface, expressed as a Fourier series in terms of dimensionless coordinates, is given by

$$\frac{\rho_s^2(z)}{R_0^2} = \sum_{n=1}^{\infty}\left[a_{2n}\cos\left(\frac{(2n-1)\pi}{2}\frac{z - z_{sh}}{z_0}\right) + a_{2n+1}\sin\left(\frac{2n\pi}{2}\frac{z - z_{sh}}{z_0}\right)\right], \tag{11}$$

where $\rho_s^2(z)$ represents the distance from a surface point to the symmetry $z$-axis and $R_0 = 1.2A^{1/3}$ fm is the radius of the corresponding spherical shape with the same volume. The shape extends along the symmetry axis by $2z_0$, with the left and right ends located at $z_{min} = z_{sh} - z_0$ and $z_{max} = z_{sh} + z_0$, respectively. Here, $z_0$ is half the extension of the shape along the symmetry axis, as derived from volume conservation, while $z_{sh}$ is determined to ensure that the center of mass of the nuclear shape lies at the origin of the coordinate system. Following the convergence properties discussed in Ref. [7], we retain the first five orders $a_2, \dots, a_6$ as a starting point and transform the parameters $a_n$ into the deformation parameters $q_n$ as follows:

$$
\begin{aligned}
q_2 &= a_2^{(0)}/a_2 - a_2/a_2^{(0)}, \\
q_3 &= a_3, \\
q_4 &= a_4 + \sqrt{(q_2/9)^2 + (a_4^{(0)})^2}, \\
q_5 &= a_5 - (q_2 - 2)a_3/10, \\
q_6 &= a_6 - \sqrt{(q_2/100)^2 + (a_6^{(0)})^2},
\end{aligned}
\tag{12}
$$

where $a_n^{(0)}$ represents the Fourier coefficients for the spherical shape. Although the higher-order coordinates $q_5$ and $q_6$ are typically negligible within the accuracy of the current approach, the set of $q_i$ possesses explicit physical significance in characterizing the nuclear fission process. In particular, $q_2$ denotes the elongation of the nucleus; $q_4$ represents the neck parameter; and $q_3$ represents the left-right asymmetry parameter. In this study, the dynamic process of nuclear fission was modeled in a three-dimensional deformation space $(q_2, q_3; q_4)$ using Fourier shape parameterization. Notably, the present work does not consider non-axially symmetric shapes because they primarily play a significant role near the ground state and first saddle point.

### 2.3 Mass distributions

In previous studies, the use of Wigner functions to approximate the probability distribution associated with the neck and mass asymmetry degrees of freedom showed good agreement between the model predictions and experimental results [7, 48, 50–52]. Based on these ideas, this study proposes a fission dynamics scenario in which the motion toward fission primarily occurs along the $q_2$ direction, accompanied by fast vibrations in the perpendicular $q_3$ and $q_4$ collective variables. The total eigenfunction $\psi_{nE}(q_2, q_3, q_4)$ of the fissioning nucleus is approximated as the product of two functions:

$$\psi_{nE}(q_2, q_3, q_4) = \mu_{nE}(q_2)\phi_n(q_3, q_4; q_2). \tag{13}$$

In this expression, $\mu_{nE}(q_2)$ depends mainly on a single variable $q_2$ and describes the motion toward fission, while $\phi_n(q_3, q_4; q_2)$ simulates $n$-phonon fast collective vibrations on the perpendicular two-dimensional plane $q_3, q_4$ for a given elongation $q_2$. For low-energy fission, only the lowest-energy eigenstate $\phi_{n=0}$ was considered.

The probability density $W(q_3, q_4; q_2)$ of finding the system for a given elongation $q_2$ within the area $(q_3 \pm dq_3, q_4 \pm dq_4)$ is given by

$$W(q_3, q_4; q_2) = |\psi(q_2, q_3, q_4)|^2 = |\phi_0(q_3, q_4; q_2)|^2. \tag{14}$$

To consider the fission process, a Wigner function was employed, which is given by

$$W(q_3, q_4; q_2) \propto \exp\left\{ -\frac{V(q_3, q_4; q_2) - V_{\min}(q_2)}{E_0} \right\}. \tag{15}$$

Here, $V_{\min}(q_2)$ is the minimum potential for a given elongation $q_2$, and $E_0$ is the zero-point energy, which is treated as an adjustable parameter.

To obtain the fragment mass yield for a given elongation $q_2$, the probabilities from different neck shapes, simulated by the $q_4$ parameter, were integrated as

$$w(q_3; q_2) = \int W(q_3, q_4; q_2) \mathrm{d}q_4. \tag{16}$$

Based on the concepts introduced in Ref. [51], the neck rupture probability $P$ was assumed to be equal to

$$P(q_3, q_4, q_2) = \frac{k_0}{k} P_{\text{neck}}(R_{\text{neck}}), \tag{17}$$

where $k$ represents the momentum in the direction toward fission and the constant parameter $k_0$ is a scaling parameter. $R_{\text{neck}}$ is the deformation-dependent neck radius, and $P_{\text{neck}}$ is a geometrical factor that indicates the probability of neck rupture, which is proportional to the neck thickness. The expression for the geometrical probability factor $P_{\text{neck}}(R_{\text{neck}})$ can be chosen arbitrarily to some extent, such as using Fermi, Lorentz, or Gaussian functions [52]. In this study, the following Gaussian form was adopted:

$$P_{\text{neck}}(R_{\text{neck}}) = \exp[-\ln 2 (R_{\text{neck}}/d)^2], \tag{18}$$

where $d$ represents the half-width of the probability distribution and is treated as another adjustable parameter in this analysis. The momentum $k$ in Eq. (17) simulates the dynamics of the fission process, which depends on both the local collective kinetic energy $E - V(q_2)$ and inertia toward the leading variable $q_2$.

$$\frac{\hbar^2 k^2}{2\overline{M}(q_2)} = E_{\text{kin}} = E - Q - V(q_2), \tag{19}$$

where $\overline{M}(q_2)$ represents the average inertia over the degrees of freedom $q_3$ and $q_4$ at a given elongation $q_2$, and $V(q_2)$ denotes the average potential. Here, the portion of the total energy converted into heat, denoted by $Q$, is assumed negligibly small. The inertia $\overline{M}(q_2)$ can be conveniently approximated by employing the irrotational flow mass parameter $B_{\text{irr}}$ [53], which is initially expressed as a function of the single collective parameter $R_{12}$ that represents the distance between fragments and the reduced mass $\mu$ of both fragments

$$\overline{M}(q_2) = \mu[1 + 11.5(B_{\text{irr}}/\mu - 1)]\left(\frac{\partial R_{12}}{\partial q_2}\right)^2. \tag{20}$$

To incorporate the neck rupture probability $P(q_3, q_4; q_2)$ into Eq. (17), the integral of the probability distribution in

Eq. (15) with respect to $q_4$ must be reformulated. This is achieved by the following expression:

$$w(q_3;q_2) = \int W(q_3, q_4;q_2)P(q_2, q_3, q_4)\mathrm{d}q_4. \tag{21}$$

The aforementioned approximation implies a crucial observation: For a fixed $q_3$ value, fission may occur within a specific range of $q_2$ deformations, each associated with different probabilities. To obtain the accurate fission probability distribution $w'(q_3;q_2)$ at a particular $q_2$ value, fission events that occurred in previous configurations with $q_2' < q_2$ must be excluded by applying the following expression:

$$w'(q_3;q_2) = w(q_3;q_2)\frac{1 - \int_{q_2'<q_2} w(q_3;q_2')\mathrm{d}q_2'}{\int w(q_3;q_2')\mathrm{d}q_2'}. \tag{22}$$

The normalized mass yield was obtained as the sum of the partial yields at different values of $q_2$.

$$Y(q_3) = \frac{\int w'(q_3;q_2)\mathrm{d}q_2}{\int w'(q_3;q_2)\mathrm{d}q_3\mathrm{d}q_2}. \tag{23}$$

Because the scaling parameter $k_0$ introduced in Eq. (17) does not appear in the definition of the mass yield, the only free parameters, the zero-point energy parameter $E_0$ in Eq. (14) and half-width parameter $d$ appear in the probability of neck rupture (18). Based on the successful reproduction of the experimental fragment mass yields in the low-energy fission of Pt to Ra isotopes, the values of the free parameters used in this study were $d = 0.16R_0$ and $E_0 = 2.2$ MeV [48].

## 3 Potential energy

In this study, the potential energy of the system was computed using the macroscopic-microscopic approach. The total energy of a nucleus with a specific deformation, represented as $E_{\mathrm{total}}(N, Z, q_n)$, was determined using the following procedure:

$$E_{\mathrm{total}}(N, Z, q_n) = E_{\mathrm{LD}}(N, Z) + E_{\mathrm{B}}(N, Z, q_n). \tag{24}$$

In the calculation, the total energy $E_{\mathrm{total}}(N, Z, q_n)$ is composed of two main contributions. The first term, denoted as $E_{\mathrm{LD}}(N, Z)$, corresponds to the macroscopic energy calculated using the standard liquid drop model and considers the proton number $Z$ and neutron number $N$ [54]. The second term, $E_{\mathrm{B}}(N, Z, q_n)$, is related to the shape parameters $q_2, q_3, q_4$ and represents the potential energy surface. In the current calculation, we focused solely on the energy term and neglected other contributions to the total energy.

$$\begin{aligned} E_{\mathrm{B}}(N, Z, q_n) = E_{\mathrm{def}}(N, Z, q_n) + E_{\mathrm{shell}}(N, Z, q_n). \\ + E_{\mathrm{pair}}(N, Z, q_n) \end{aligned} \tag{25}$$

The deformation correction energy $E_{\mathrm{def}}(N, Z, q_2, q_3, q_4)$ was obtained from the tables in Ref. [55]. The microscopic terms consist of the shell correction energy $E^{\nu(\pi)}_{\mathrm{shell}}(N, Z, \{\varepsilon_i\}, q_2, q_3, q_4)$ proposed by Strutinsky [56, 57] and pairing interaction energy $E^{\nu(\pi)}_{\mathrm{pair}}(N, Z, \{\varepsilon_i\}, q_2, q_3, q_4)$ calculated using Eq. (1), where $\nu$ $(\pi)$ represents the label of the neutron (proton) sector. The microscopic calculations considered 18 deformed harmonic oscillator shells in the Yukawa-folded single-particle potential to determine the single-particle energy levels. Additionally, for the pairing correction energy, 66 single-particle levels around the neutron Fermi level and 51 single-particle levels around the proton Fermi level were considered. To determine the overall potential energy surface, a multidimensional minimization process was performed by simultaneously considering all axial degrees of freedom. This included minimizing the elongation of the nucleus $q_2$, asymmetry of the left and right mass fragments $q_3$, and size of the neck $q_4$. The nuclear shape and energy landscape can be comprehensively understood by considering all these degrees of freedom together.

Figure 1 illustrates the behavior of the potential energy surface (PES) during the fission of $^{240}$Pu. At the initial stage of fission, $q_2 < 0.5$, the PES exhibits a very soft octupole deformation, and its minimum (ground state) occurs at $q_3 = 0$. The fission barrier heights obtained from the present model are consistent with the corresponding experimental results from Ref. [58]. In particular, the inner and outer barrier heights were 4.88 MeV and 5.24 MeV, respectively, and the corresponding experimental results were

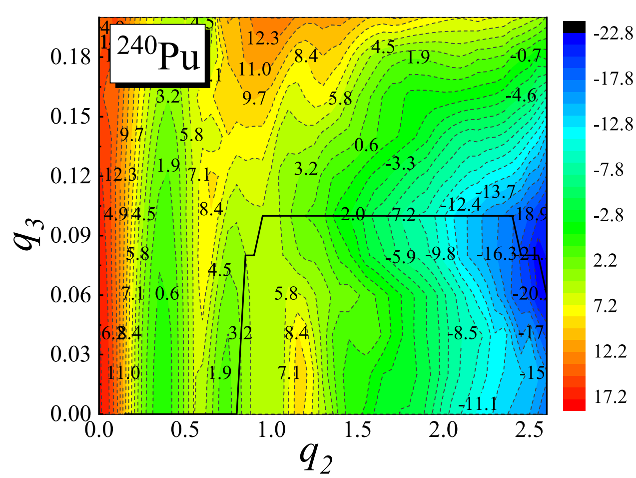


**Fig. 1** (Color online) Contour map of the PES of the nucleus $^{240}$Pu (in MeV), minimized $q_4$ with the pairing interaction strength $G^{\nu} = 0.08$ and $G^{\pi} = 0.10$ (in MeV). The black trajectory shows the static fission path

5.80 MeV and 5.30 MeV, respectively. Furthermore, in the asymmetric fission path, Fig. 1 exhibits a plateau at high deformation, followed by a cliff (asymmetric scission point: $q_2 = 2.45, q_3 = 0.10, q_4 = -0.09$).

The strength of the pairing interaction $G$ is typically determined using empirical formulas or by fitting experimental data such as odd-even mass differences [59–62]. Previous studies have demonstrated that pairing is crucial in the inner and outer barrier regions. Furthermore, the first and second saddle points are highly sensitive to the strength of the pairing interaction [34, 63, 64]. Therefore, in the present model, experimental observables, such as the odd-even mass difference (reflecting ground-state properties) and barrier heights (reflecting excited-state properties), were used to determine the experimental values of the pairing interaction strength during fission.

In this study, realistic values of the pairing interaction strengths for the isotopic chains of Th, U, Pu, and Cm were obtained by fitting the experimental values of the odd-even mass difference and heights of the inner and outer barriers. The odd–even mass difference was calculated using the following three-point formula:

$$P(A) = E_{\text{total}}(N+1,Z) + E_{\text{total}}(N-1,Z) - 2E_{\text{total}}(N,Z). \tag{26}$$

The odd-even mass difference is attributed to the presence of nucleonic pairing interactions and is highly sensitive to changes in the pairing interaction strength $G$ [65]. The corresponding values of $G^{\nu}$ ($G^{\pi}$) are listed in Table 1.

Figure 2 clearly shows that the odd-even mass differences obtained using the proposed approach closely match the experimental data for the Th, U, Pu, and Cm isotopes. In addition, as shown in Fig. 3, the inner (a) and outer (b) fission barriers for the Th, U, Pu, and Cm isotopes calculated using the current model, exhibit remarkable agreement with the corresponding experimental values. It is necessary to indicate that the theoretical inner barrier heights of light Th isotopes in Fig. 3a are systematically lower than the experimental data, which has also been reported in other calculations for light actinides in Refs. [12, 13, 66–68]. Based on the analysis of the different effects of the neutron and proton pairing interactions on the inner and outer barrier heights in Ref. [32], the above results may be related to the strong

**Table 1** Pairing interaction strength $G^{\nu}$ ($G^{\pi}$) (in MeV) for Th, U, Pu, and Cm isotopes

| | Th | U | Pu | Cm |
|---|---|---|---|---|
| $G^{\nu}$ | 0.096 | 0.080 | 0.080 | 0.096 |
| $G^{\pi}$ | 0.120 | 0.100 | 0.100 | 0.120 |

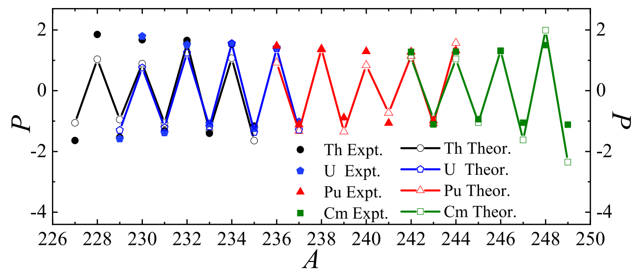


**Fig. 2** (Color online) Odd–even mass differences (in MeV) for the Th, U, Pu, and Cm isotopes. The experimental values and theoretical values calculated using the present model are denoted as "Expt." and "Theor.", respectively. Experimental data are taken from Ref. [65] (in MeV)

neutron pairing interaction strength. In this study, the pairing interaction strength values in Table 1 were set to $G_0^{\nu}$ ($G_0^{\pi}$) for the Th, U, Pu, and Cm isotopes.

## 4 Effect of the pairing interaction on the fragment mass distributions of $^{230}$Th, $^{234}$U, $^{240}$Pu, and $^{246}$Cm

Investigation of the dynamics around fission structures is crucial for comprehending various aspects of the final fission state, such as the kinetic energy and mass distributions [7, 69, 70]. In this study, the fission fragment mass distribution of $^{240}$Pu was calculated based on its PES and compared with the experimental data [71].

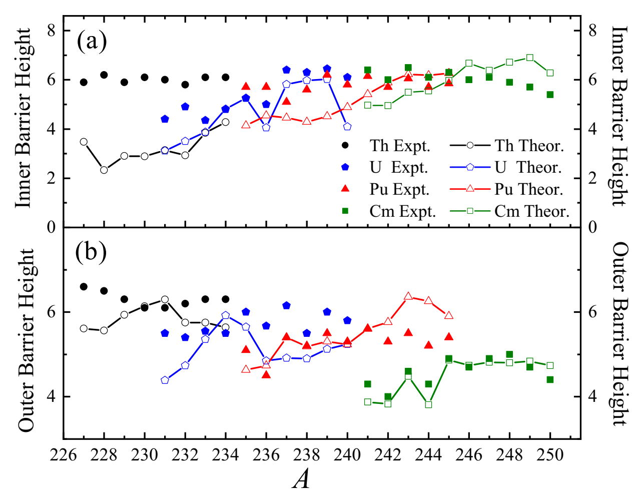


**Fig. 3** (Color online) Inner (**a**) and outer (**b**) fission barriers for Th, U, Pu, and Cm isotopes. The theoretical values obtained using the present model and experimental values are labeled as "Theor." and "Expt.", respectively. The experimental data (in MeV) is sourced from Ref. [12]. The the typical uncertainty in the experimental values, which is estimated based on variations among different compilations, is approximately ±0.5 MeV [12]

Figure 4 shows the reasonable agreement between the calculated results and experimental data [71]. Moreover, the obtained fission fragment mass distribution aligns with the understanding that the static fission in $^{240}$Pu is predominantly asymmetric, as indicated by the fission PES. During the calculation, a Gaussian folded function with a full width at half maximum of 4.9u [72] was employed to determine the mass yields. In addition, the zero-point energy parameter $E_0 = 2.2$ MeV and half-width parameter $d = 1.6$ fm [48], were utilized.

In the case of fission nuclei, each elongation deformation variable $q_2$ corresponds to a distribution of the fragment mass numbers $A_f$ of the nuclear fragments produced during fission. Figure 5 illustrates the distribution of fragment mass numbers for $^{240}$Pu. Fission predominantly occurs in the region of asymmetric fission, with the corresponding mass numbers of the heavy fragments centered around $A \approx 141$. The scission point, which represents the point of fragment separation, is located at $q_2 = 2.3$. Only a small proportion of the fragments undergo symmetrical fission.

To investigate the influence of the pairing interaction on the fission fragment mass distribution in the current model, we calculated the yield of the fission fragment as a function of the mass number ($A_f$) for $^{230}$Th, $^{234}$U, $^{240}$Pu, and $^{246}$Cm with different pairing interaction strengths. The results presented in Fig. 6 indicate that for these nuclei, the two asymmetric peaks of the theoretical yield are significantly reduced, while the symmetric valley becomes more prominent as the pairing interaction strength $G$ increases from $80\%G_0$ to $120\%G_0$. Similar observations were reported for a three-dimensional Langevin model based on the BCS approximation [73]. These findings suggest that the fragment mass distribution is sensitive to variations in the pairing interaction strength and highlight the significant role of pairing interactions in determining the fragment mass distribution for $^{230}$Th, $^{234}$U, $^{240}$Pu, and $^{246}$Cm. Furthermore, when the pairing interaction strength $G$ is $120\%G_0$, the theoretical calculations closely match the experimental data for the fragment mass distributions of $^{230}$Th, $^{234}$U, and $^{240}$Pu. However, for $^{246}$Cm, the calculated results align better with the experimental values when the pairing interaction strength is $80\%G_0$.

Figure 7 illustrates the calculated odd-even mass differences at the asymmetric and symmetric fission points for $^{230}$Th, $^{234}$U, $^{240}$Pu, and $^{246}$Cm, considering the variation in the

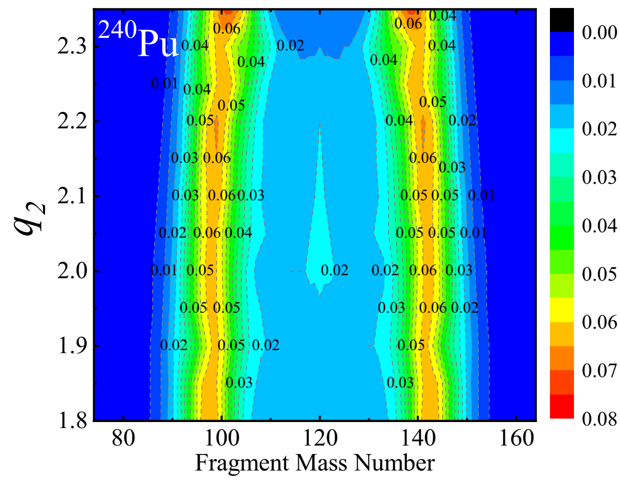


**Fig. 5** (Color online) Mass yield of $^{240}$Pu as a function of the mass number $A_f$ and elongation deformation $q_2$

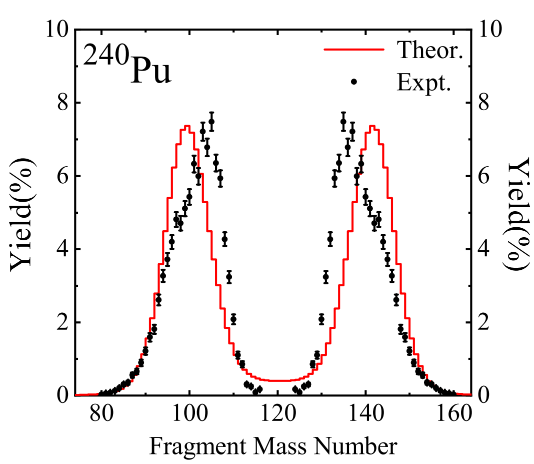


**Fig. 4** (Color online) Mass yield of $^{240}$Pu and comparison with the experimental data [71]

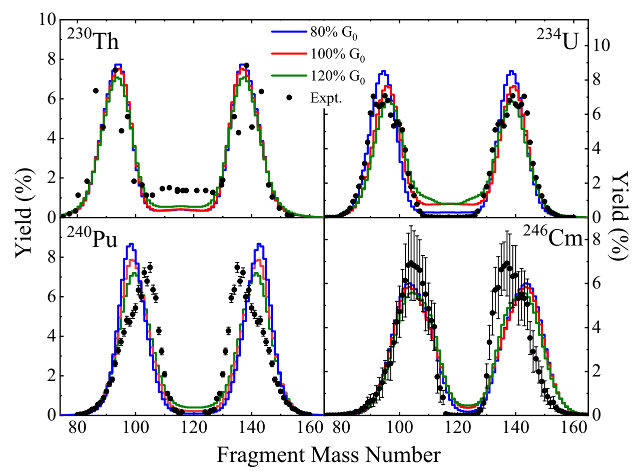


**Fig. 6** (Color online) Mass yields for $^{230}$Th, $^{234}$U, $^{240}$Pu, and $^{246}$Cm as a function of mass numbers ($A_f$) with varying pairing interaction strengths. The experimental data for $^{230}$Th are extracted from the charge-yields as reported in Ref. [64]. The mass yields for $^{234}$U are obtained from Ref. [74]. For $^{240}$Pu, the calculated mass yields are compared with experimental data [71]. The experimental data for $^{246}$Cm are taken from Ref. [75]

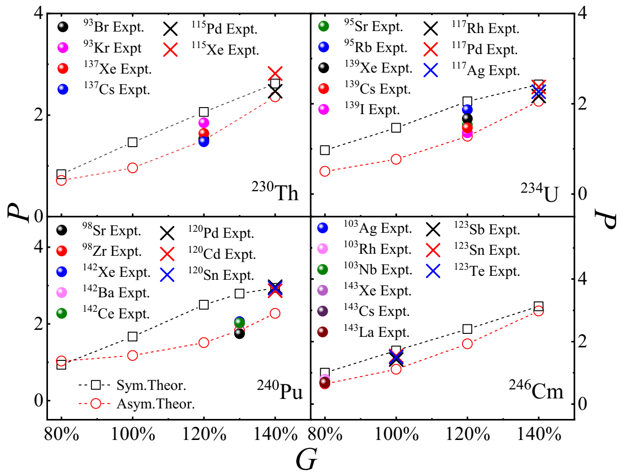

**Fig. 7** (Color online) Odd–even mass differences (in MeV) of $^{230}$Th, $^{234}$U, $^{240}$Pu, and $^{246}$Cm at the asymmetric and the symmetric scission points for pairing interaction strengths $G^{\nu(\pi)}$ varying from 80%$G_0$ to 120%$G_0$ (in MeV). The theoretical values calculated in the present model based on Eq. (26) in Ref. [60] are represented as "Sym. Theor." and "Asym. Theor." for the symmetric and asymmetric points, respectively. The experimental values of the odd-even mass difference for asymmetric and symmetric fission fragments of $^{230}$Th, $^{234}$U, $^{240}$Pu, and $^{246}$Cm denoted as "Expt." are obtained from Ref. [65] (in MeV)

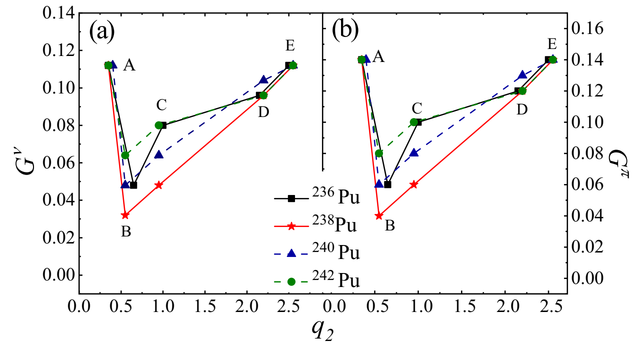

**Fig. 8** (Color online) Pairing interaction strength $G^{\nu}$ ($G^{\pi}$) (in MeV) obtained by fitting the ground-state binding energy, inner and outer barrier heights, and fragment mass distribution calculations for $^{236-242}$Pu isotopes. Points **A**–**E** represent the corresponding $q_2$ values for the ground-state binding energy, inner and outer barrier heights, and the asymmetric and symmetric scission points, respectively

pairing strength $G$ ranging from 80%$G_0$ to 120%$G_0$. In this analysis, it was assumed that the ground-state odd-even mass differences represented the odd-even binding-energy differences in the scission configuration, despite some shape differences. A comparison of the experimental odd-even mass differences of asymmetric and symmetric fission fragments in nuclei such as $^{230}$Th, $^{234}$U, $^{240}$Pu, and $^{246}$Cm indicates that the calculated results exhibit better agreement with experimental values at the asymmetric fission point when the pairing strength is set to 120%$G_0$ for $^{230}$Th, $^{234}$U, and $^{240}$Pu. Conversely, a stronger pairing interaction is required at the symmetric fission point, and the calculated results agree better with the experimental values when the pairing strength is set to 140%$G_0$ for $^{230}$Th, $^{234}$U, and $^{240}$Pu. The calculated results for the odd-even mass differences at the symmetric and asymmetric fission points for $^{246}$Cm demonstrated that the pairing strengths of 80%$G_0$ and 120%$G_0$ are consistent with experimental values. This finding agrees with the earlier conclusion that the fission fragment masses for $^{230}$Th, $^{234}$U, and $^{240}$Pu are better distributed when the pairing interaction strength increases.

The calculations presented above suggest that different elongation deformations of the nuclei require different pairing interaction strengths to provide a better description of the fission products. By fitting the ground-state binding energy, inner and outer barrier heights, and mass distribution calculations for the Pu isotopes, the optimal values for the strength of the pairing interactions were determined. As shown in Fig. 8, the strength of the pairing interactions varies nonlinearly with increasing elongation deformation of the nucleus. Compared to the barrier height, a stronger interaction is required to accurately describe the fragment mass distribution.

## 5 Fragment mass distribution of Th, U, Pu, and Cm isotopes

Based on the above results, we calculated the fragment mass distributions of the Th, U, Pu, and Cm isotope chains based on the corresponding PES, with the pairing interaction strength set to 120%$G_0$. The theoretical calculations presented in Fig. 9 are consistent with the experimental data for all the isotopes. The peak height, width, and position of the fragment mass distribution closely match the experimental data. However, some discrepancies are observed for specific isotopes, which can be attributed to the limitations of the available experimental data.

For $^{228}$Th and $^{230}$Th, the experimental data for the fragment mass distribution were obtained by converting the charge distribution of the fragments at an excitation energy of 11 MeV in the fission system [64]. This may explain why the experimental value of the asymmetric mass yield of $^{228}$Th is lower than the theoretical value, whereas the symmetric fission yield is relatively high. The experimental data from thermal-neutron-induced fission were used for $^{234}$U and $^{236}$U [74]. The theoretical results show a higher symmetric valley for $^{234}$U compared to that for the experimental data. Owing to the lack of available experimental data for $^{238}$U, the evaluated post-neutron data from ENDF/B-VIII.0 were utilized [75].

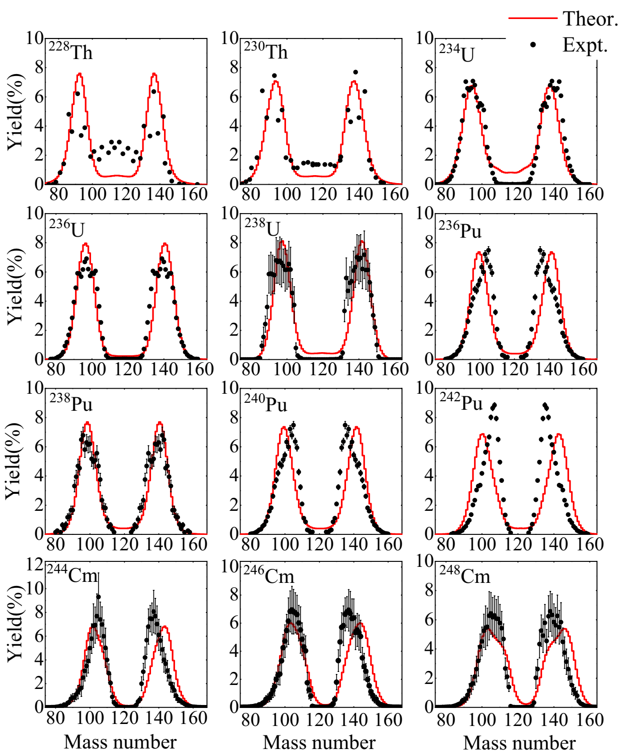


**Fig. 9** (Color online) Mass yields for Th, U, Pu, and Cm isotopes as a function of the mass numbers ($A_{\mathrm{f}}$). The theoretical values calculated using the present model are represented as "Theor." while the experimental data are denoted as "Expt." [74]. The experimental data for $^{228}$Th and $^{230}$Th are obtained by converting the charge distribution with an excitation energy of 11 MeV [64]. For the isotopes $^{234}$U, $^{236}$U, and $^{242}$Pu, the experimental data used are from thermal neutron-induced fission [76], while for $^{236}$Pu, $^{238}$Pu, and $^{240}$Pu, the data are from spontaneous fission experiments [75]. The evaluated post-neutron data for $^{238}$U and $^{244-248}$Cm are taken from ENDF/B-VIII.0 [75]

Experimental data from spontaneous fission were used for $^{236}$Pu, $^{238}$Pu, and $^{240}$Pu, and the calculated results closely matched the experimental data in terms of the peak width. For $^{242}$Pu, experimental data from thermal neutron-induced fission were employed. The calculated results exhibited a similar peak width, but deviated from the experimental data by 2–3 mass units in the peak position. For the $^{244-248}$Cm isotopes, the evaluated post-neutron data from ENDF/B-VIII.0 were used. The calculated results presented in Fig. 9 are consistent with the experimental data, indicating the effectiveness of the proposed model in reproducing the fission fragment mass distribution.

Overall, the model employed in this study successfully reproduced the experimental data of the fission fragment mass distribution for Th, U, Pu, and Cm isotopes, providing a valuable tool for understanding and analyzing fission processes.

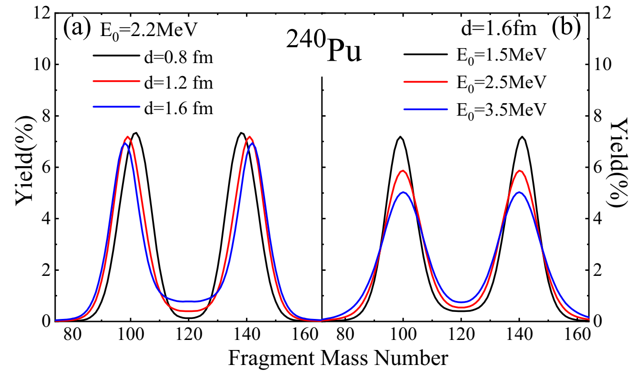


**Fig. 10** (Color online) Mass yields of $^{240}$Pu for different values of the zero-point energy $E_0$ in Eq. (15) and half-width parameter $d$ in Eq. (18)

## 6 Effects of model parameters on the fragment mass distribution of $^{240}$Pu

In subsequent studies, the effects of the zero-point energy $E_0$ in Eq. (15) and half-width parameter $d$ in Eq. (18) of the three-dimensional collective model on the fragment mass distribution of $^{240}$Pu were investigated. The results (Fig. 10a) indicate that the half-width parameter $d$ primarily influences the position of the asymmetric peak. The position of the asymmetric peak shifts toward larger fragment masses as the half-width parameter $d$ increases.

However, the zero-point energy $E_0$ primarily affected the peak value of the fission fragments. As shown in Fig. 10b, the asymmetric peak value of the fission fragment mass distribution decreases with increasing zero-point energy $E_0$. These observations are consistent with findings reported in the literature [7]. These results highlight the importance of considering the zero-point energy and half-width parameter in the three-dimensional collective model for a more accurate description of the fragment mass distribution in fission processes.

## 7 Conclusion

In summary, this article presents a comprehensive analysis of the fission process in Th, U, Pu, and Cm isotopes using a Yukawa-Folded mean-field plus standard pairing model. The PES, fission paths, barriers, and fragment mass distributions were calculated using a macroscopic-microscopic framework. This study focused on investigating the impact of pairing interactions on the mass distribution of fission fragments.

Our results demonstrate that pairing interactions play a crucial role in shaping the fission process of $^{230}$Th, $^{234}$U,

$^{240}$Pu, and $^{246}$Cm. The strength of the pairing interaction was determined by fitting the experimental data of odd-even mass differences and barrier heights, which led to better agreement between theory and experiment. Furthermore, we found that the fission fragment mass distribution was highly sensitive to changes in the pairing interaction strengths for $^{230}$Th, $^{234}$U, $^{240}$Pu, and $^{246}$Cm. Stronger pairing interactions favored symmetric fission, whereas weaker interactions led to more asymmetric fission. The odd–even mass differences for $^{230}$Th, $^{234}$U, $^{240}$Pu, and $^{246}$Cm at the symmetric and asymmetric fission points were compared with experimental values, providing additional support for the findings regarding the role of the pairing interaction.

Moreover, a comparison of our theoretical calculations with the experimental data confirmed the accuracy of our model in describing the fission fragment mass distributions for Th, U, Pu, and Cm isotopes. The peak heights, widths, and positions of the fragment mass distributions were reproduced well, demonstrating the effectiveness of the proposed approach.

In addition, we explored the effects of the zero-point energy and half-width parameter on the fragment mass distribution for $^{240}$Pu. The zero-point energy primarily influenced the peak value of the fission fragments, while the half-width parameter affected the position of the asymmetric peak.

In conclusion, this study contributes to the understanding of the fission process by emphasizing the crucial role of pairing interactions and their relationship with nuclear elongation. The consistency between the theoretical calculations and experimental data, along with the analysis of additional parameters, strengthen the validity and applicability of the proposed model. The insights gained from this study can guide future investigations in the field of nuclear fission, and advance our understanding of this fundamental process.

**Author Contributions** All authors contributed to the study conception and design. Material preparation, data collection and analysis were performed by Jin-Huan Zheng, Mei-Yan Zheng and Xin Guan. The first draft of the manuscript was written by Xin Guan and all authors commented on previous versions of the manuscript. All authors read and approved the final manuscript.

**Data availability** The data that support the findings of this study are openly available in Science Data Bank at https://www.doi.org/10.57760/sciencedb.j00186.00270 and https://cstr.cn/31253.11.sciencedb.j00186.00270.

## Declarations

**Conflict of interest** The authors declare that they have no conflict of interest.

## References

1. M. Bender, R. Bernard, G. Bertsch et al., Future of nuclear fission theory. J. Phys. G Nuclear Part. Phys. **47**(11), 113002 (2020). https://doi.org/10.1088/1361-6471/abab4f
2. A. Bulgac, Fission-fragment excitation energy sharing beyond scission. Phys. Rev. C **102**, 044609 (2020). https://doi.org/10.1103/PhysRevC.102.044609
3. A. Bulgac, P. Magierski, K.J. Roche et al., Nuclear reactions and superfluid time dependent density functional theory. Phys. Rev. Lett. **116**, 122504 (2016). https://doi.org/10.2174/9781681087641119020008
4. J. Zhao, T. Nikšić, D. Vretenar et al., Time-dependent generator coordinate method study of fission: mass parameters. Phys. Rev. C **101**, 064605 (2020). https://doi.org/10.1103/PhysRevC.101.064605
5. J.C. Pei, W. Nazarewicz, J.A. Sheikh et al., Fission barriers of compound superheavy nuclei. Phys. Rev. Lett. **102**, 192501 (2009). https://doi.org/10.1103/PhysRevLett.102.192501
6. K.H. Schmidt, B. Jurado, Review on the progress in nuclear fission-experimental methods and theoretical descriptions. Rep. Prog. Phys. **81**, 106301 (2018). https://doi.org/10.1088/1361-6633/aacfa7
7. K. Pomorski, A. Dobrowolski, R. Han et al., Mass yields of fission fragments of Pt to Ra isotopes. Phys. Rev. C **101**, 064602 (2020). https://doi.org/10.1103/PhysRevC.101.064602
8. M.R. Mumpower, P. Jaffke, M. Verriere et al., Primary fission fragment mass yields across the chart of nuclides. Phys. Rev. C **101**, 054607 (2020). https://doi.org/10.1103/PhysRevC.101.054607
9. H.J. Krappe, K. Pomorski, *Theory of Nuclear Fission*, Lecture Notes in Physics, vol. 838. (Springer, Berlin, 2012)
10. K. Rutz, M. Bender, P. Reinhard et al., Pairing gap and polarisation effects. Phys. Lett. B **468**, 1 (1999). https://doi.org/10.1016/S0370-2693(99)01190-9
11. N. Schunck, D. Duke, H. Carr et al., Description of induced nuclear fission with Skyrme energy functionals: Static potential energy surfaces and fission fragment properties. Phys. Rev. C **90**, 054305 (2014). https://doi.org/10.1103/PhysRevC.90.054305
12. M. Samyn, S. Goriely, J.M. Pearson, Further explorations of Skyrme-Hartree-Fock-Bogoliubov mass formulas. V. Extension of the fission barriers. Phys. Rev. C **72**, 044316 (2005). https://doi.org/10.1103/PhysRevC.72.044316
13. H. Abusara, A.V. Afanasjev, P. Ring, Fission barriers in actinides in covariant density functional theory: the role of triaxiality. Phys. Rev. C **82**, 044303 (2010). https://doi.org/10.1103/PhysRevC.82.044303
14. S. Karatzikos, A.V. Afanasjev, G.A. Lalazissis et al., The fission barriers in Actinides and superheavy nuclei in covariant density functional theory. Phys. Lett. B **689**, 72 (2010). https://doi.org/10.1016/j.physletb.2010.04.045
15. J. Sadhukhan, J. Dobaczewski, W. Nazarewicz et al., Pairing-induced speedup of nuclear spontaneous fission. Phys. Rev. C **90**, 061304(R) (2014). https://doi.org/10.1103/PhysRevC.90.061304
16. W. Tsung-shyh, T. Chin-yen, The influences of pairing force on the properties of actinide nuclei. Acta Phys. Sin. **21**(5), 915 (1965). https://doi.org/10.7498/aps.21.915
17. Y. Zhu, T. Lee, M. Lee, The pairing effects of nuclei on the angular distribution of the fission fragments. Acta Phys. Sin. **22**(2), 136 (1966). https://doi.org/10.7498/aps22.136
18. Q.-F. Song, L. Zhu, H. Guo et al., Verification of neutron-induced fission product yields evaluated by a tensor decompsition model in transport-burnup simulations. Nucl. Sci. Tech. **34**, 32 (2023). https://doi.org/10.1007/s41365-023-01176-5
19. L. Zhou, S.-M. Wang, D.-Q. Fang et al., Recent progress in two-proton radioactivity. Nucl. Sci. Tech. **33**, 105 (2022). https://doi.org/10.1007/s41365-022-01091-1

20. X.-C. Ming, H.-F. Zhang, X. Rui-Rui et al., Nuclear mass based on the multi-task learning neural network method. Nucl. Sci. Tech. **33**, 48 (2022). https://doi.org/10.1007/s41365-022-01031-z
21. Y.-F. Gao, B.-S. Cai, C.-X. Yuan, Investigation of $\beta^{-}$-decay half-life and delayed neutron emission with uncertainty analysis. Nucl. Sci. Tech. **34**, 9 (2023). https://doi.org/10.1007/s41365-022-01153-4
22. H. Goutte, J.F. Berger, P. Casoli et al., Microscopic approach of fission dynamics applied to fragment kinetic energy and mass distributions in $^{238}$U. Phys. Rev. C **71**, 024316 (2005). https://doi.org/10.1103/PhysRevC.71.024316
23. J. Sadhukhan, W. Nazarewicz, N. Schunck, Microscopic modeling of mass and charge distributions in the spontaneous fission of $^{240}$Pu. Phys. Rev. C **93**, 011304(R) (2016). https://doi.org/10.1103/PhysRevC.93.011304
24. H. Tao, J. Zhao, Z.P. Li et al., Microscopic study of induced fission dynamics of $^{226}$Th with covariant energy density functionals. Phys. Rev. C **96**, 024319 (2017). https://doi.org/10.1103/PhysRevC.96.024319
25. Z. Matheson, S.A. Giuliani, W. Nazarewicz et al., Cluster radioactivity of $^{294}_{118}$Og$_{176}$. Phys. Rev. C **99**, 041304(R) (2019). https://doi.org/10.1103/PhysRevC.99.041304
26. Z. Łojewski, A. Staszczak, Role of pairing degrees of freedom and higher multipolarity deformations in spontaneous fission process. Nucl. Phys. A **657**, 134 (1999). https://doi.org/10.1016/S0375-9474(99)00328-0
27. M. Mirea, R.C. Bobulescu, Cranking mass parameters for fission. J. Phys. G **37**, 055106 (2010). https://doi.org/10.1088/0954-3899/37/5/055106
28. S.A. Giuliani, Z. Matheson, W. Nazarewicz et al., Colloquium: superheavy elements: oganesson and beyond. Rev. Mod. Phys. **91**, 011001 (2019). https://doi.org/10.1103/RevModPhys.91.011001
29. J. Zhao, B.-N. Lu, T. Nikšić et al., Multidimensionally constrained relativistic mean-field study of spontaneous fission: Coupling between shape and pairing degrees of freedom. Phys. Rev. C **93**, 044315 (2016). https://doi.org/10.1103/PhysRevC.93.044315
30. J. Zhao, T. Nikšić, D. Vretenar, Microscopic self-consistent description of induced fission: dynamical pairing degree of freedom. Phys. Rev. C **104**, 044612 (2021). https://doi.org/10.1103/PhysRevC.104.044612
31. Y. Qiang, J.C. Pei, P.D. Stevenson, Fission dynamics of compound nuclei: pairing versus fluctuations. Phys. Rev. C **103**, L031304 (2021). https://doi.org/10.1103/PHYSREVC.103.L031304
32. X. Guan, C. Qi, An iterative approach for the exact solution of the pairing Hamiltonian. Comp. Phys. Comm. **275**, 108310 (2022). https://doi.org/10.1016/j.cpc.2022.108310
33. X.Y. Liu, C. Qi, X. Guan et al., PairDiagSph: generalization of the exact pairing diagonalization program for spherical systems. Comp. Phys. Comm. **263**, 1107897 (2021). https://doi.org/10.1016/j.cpc.2021.107897
34. X. Guan, Y. Xin, Y.J. Chen et al., Impact of the pairing interaction on fission in the deformed mean-field puls standard pairing model. Phys. Rev. C **104**, 044329 (2021). https://doi.org/10.1103/PhysRevC.104.044329
35. X. Guan, T.C. Wang, W.Q. Jiang et al., Impact of the pairing interaction on fission of U isotopes. Phys. Rev. C **107**, 034307 (2023). https://doi.org/10.1103/PhysRevC.107.034307
36. R. W. Richardson, A restricted class of exact eigenstates of the pairing-force Hamiltonian. Phys. Lett. **3**, 277 (1963). https://doi.org/10.1016/0031-9163(63)90259-2; Application to the exact theory of the pairing model to some even isotopes of lead. Phys. Lett. **5**, 82 (1963). https://doi.org/10.1016/S0375-9601(63)80039-0;
37. R. W. Richardson and N. Sherman, Pairing models of Pb$^{206}$, Pb$^{204}$ and Pb$^{202}$. Nucl. Phys. **52**, 221 (1964); **52**, 253 (1964). https://doi.org/10.1016/0029-5582(64)90690-X
38. M. Gaudin, Diagonalization of a class of spin hamiltonians. J. Physique **37**, 1087 (1976). https://doi.org/10.1051/jphys:0197600370100108700
39. F. Pan, J.P. Draayer, W.E. Ormand, A particle-number-conserving solution to the generalized pairing problem. Phys. Lett. B **422**, 1 (1998). https://doi.org/10.1016/S0370-2693(98)00034-3
40. J. Dukelsky, C. Esebbag, S. Pittel, Electrostatic mapping of nuclear pairing. Phys. Rev. Lett. **88**, 062501 (2002). https://doi.org/10.1103/PhysRevLett.88.062501
41. J. Dukelsky, S. Pittel, G. Sierra, Colloquium: exactly solvable Richardson–Gaudin models for many-body quantum systems. Rev. Mod. Phys. **76**, 643 (2004). https://doi.org/10.1103/RevModPhys.76.643
42. A. Faribault, O. El Araby, C. Sträter et al., Gaudin models solver based on the correspondence between Bethe ansatz and ordinary differential equations. Phys. Rev. B **83**, 235124 (2011). https://doi.org/10.1103/PhysRevB.83.235124
43. O. El Araby, V. Gritsev, A. Faribault, Bethe ansatz and ordinary differential equation correspondence for degenerate Gaudin models. Phys. Rev. B **85**, 115130 (2012). https://doi.org/10.1103/PhysRevB.85.115130
44. X. Guan, K.D. Launey, M.X. Xie et al., Numerical algorithm for the standard pairing problem based on the Heine–Stieltjes correspondence and the polynomial approach. Comp. Phys. Commun. **185**, 2714 (2014). https://doi.org/10.1016/j.cpc.2014.05.023
45. C. Qi, T. Chen, Exact solution of the pairing problem for spherical and deformed systems. Phys. Rev. C **92**, 051304(R) (2015). https://doi.org/10.1103/PhysRevC.92.051304
46. X. Guan, K.D. Launey, M.X. Xie et al., Heine–Stieltjes correspondence and the polynomial approach to the standard pairing problem. Phys. Rev. C **86**, 024313 (2012). https://doi.org/10.1103/PhysRevC.86.024313
47. C. Schmitt, K. Pomorski, B.K. Nerlo-Pomorska et al., Performance of the Fourier shape parametrization for the fission process. Phys. Rev. C **95**, 034612 (2017). https://doi.org/10.1103/PhysRevC.95.034612
48. K. Pomorski, J.M. Blanco, P.V. Kostryukov et al., Fission fragment mass yields of Th to Rf even-even nuclei. Chin. Phys. C **45**, 054109 (2021). https://doi.org/10.1088/1674-1137/abec69
49. L.L. Liu, Y.J. Chen, X.Z. Wu et al., Analysis of nuclear fission properties with the Langevin approach in Fourier shape parametrization. Phys. Rev. C **103**, 044601 (2021). https://doi.org/10.1103/PhysRevC.103.044601
50. B. Nerlo-Pomorska, K. Pomorski, F.A. Ivanyuk, Fission fragments mass distribution of $^{236}$U. Acta Phys. Pol. B Suppl. **8**, 659 (2015). https://doi.org/10.5506/APhysPolBSupp.8.659
51. K. Pomorski, F.A. Ivanyuk, B. Nerlo-Pomorska, Mass distribution of fission fragments within the Born–Oppenheimer approximation. Eur. Phys. J. A **53**, 59 (2017). https://doi.org/10.1140/epja/i2017-12250-5
52. K. Pomorski, B. Nerlo-Pomorska, J. Bartel et al., Fission fragment mass and total kinetic energy distributions of spontaneously fissioning plutonium isotopes. Eur. Phys. J. Web Conf. **169**, 00016 (2018). https://doi.org/10.1051/epjconf/201816900016
53. J. Randrup, S.E. Larsson, P. Möller et al., Spontaneous-fission half-lives for even nuclei with $Z \geq 92$. Phys. Rev. C **13**, 229 (1976). https://doi.org/10.1103/PhysRevC.13.229
54. K. Pomorski, J. Dudek, Nuclear liquid-drop model and surface-curvature effects. Phys. Rev. C **67**, 044316 (2003). https://doi.org/10.1103/PhysRevC.67.044316

55. P. Moller, J. R. Nix, W. D. Myers et al., Nuclear ground-state masses and deformations. At. Data Nucl. Data Tables 59 and 185 (1995). https://doi.org/10.1006/adnd.1995.1002
56. V.M. Strutinsky, Shell effects in nuclear masses and deformation energies. Nucl. Phys. A **95**, 420 (1967). https://doi.org/10.1016/0375-9474(67)90510-6
57. V.M. Strutinsky, Shells in deformed nuclei. Nucl. Phys. A **122**, 1 (1968). https://doi.org/10.1016/0375-9474(68)90699-4
58. R. Capote, M. Herman, P. Obložinský et al., RIPL-reference input parameter library for calculation of nuclear reactions and nuclear data evaluations. Nucl. Data Sheets **110**, 3107 (2009). https://doi.org/10.1016/j.nds.2009.10.004
59. Y. Sun, Projection techniques to approach the nuclear many-body problem. Phys. Scr. **91**, 043005 (2016). https://doi.org/10.1088/0031-8949/91/4/043005
60. M. Bender, K. Rutz, P.-G. Reinhard et al., paired the gaps from nuclear mean-field models. Eur. Phys. J. A **8**, 59 (2000). https://doi.org/10.1007/s10050-000-4504-z
61. Y.Z. Wang, F.Z. Xing, J.P. Cui et al., Roles of tensor force and pairing correlation in two-proton radioactivity of halo nuclei. Chin. Phys. C **47**(084101), 2023 (2023). https://doi.org/10.1088/1674-1137/acd680
62. Y.Z. Wang, Y. Li, C. Qi et al., Pairing Effects on Bubble Nuclei. Chin. Phys. Lett. **36**, 032101 (2019). https://doi.org/10.1088/0256-307X/36/3/032101
63. I.V. Ryzhov, S.G. Yavshits, G.A. Tutin et al., Fragment-mass distributions in neutron-induced fission of $^{232}$Th and $^{238}$U at 33, 45, and 60 MeV. Phys. Rev. C **83**, 054603 (2011). https://doi.org/10.1103/PhysRevC.83.054603
64. K.H. Schmidt, S. Steinhuser, C. Bckstiegel, Relativistic radioactive beams: a new access to nuclear-fission studies. Nucl. Phys. A **665**, 221 (2000). https://doi.org/10.1016/S0375-9474(99)00384-X
65. U.S. National Nuclear Data Center: http://www.nndc.bnl.gov/
66. P. Möller, A.J. Sierk, T. Ichikawa et al., Heavy-element fission barriers. Phys. Rev. C **79**, 064304 (2009). https://doi.org/10.1103/PhysRevC.79.064304
67. P. Jachimowicz, M. Kowal, J. Skalski, Static fission properties of actinide nuclei. Phys. Rev. C **101**, 014311 (2020). https://doi.org/10.1103/PhysRevC.101.014311
68. A. Dobrowolski, K. Pomorski, J. Bartel, Fission barriers in a macroscopic-microscopic model. Phys. Rev. C **75**, 024613 (2007). https://doi.org/10.1103/PhysRevC.75.024613
69. N. Schunck, L.M. Robledo, Microscopic theory of nuclear fission: a review. Rep. Prog. Phys. **79**, 116301 (2016). https://doi.org/10.1088/0034-4885/79/11/116301
70. G.F. Bertsch, W. Younes, L.M. Robledo, Scission dynamics with K partitions. Phys. Rev. C **97**, 064619 (2018). https://doi.org/10.1103/PhysRevC.97.064619
71. L. Demattè, C. Wagemans, R. Barthèlèmy et al., Fragments' mass and energy characteristics in the spontaneous fission of $^{236}$Pu, $^{238}$Pu, $^{240}$Pu, $^{242}$Pu, and $^{244}$Pu. Nucl. Phys. A **617**, 331 (1997). https://doi.org/10.1016/S0375-9474(97)00032-8
72. A. Göök, F.-J. Hambsch, S. Oberstedt et al., Prompt neutrons in correlation with fission fragments from $^{235}$U($n$,$f$). Phys. Rev. C **98**, 044615 (2018). https://doi.org/10.1103/PhysRevC.98.044615
73. K. Pomorski, B. Nerlo-Pomorska, Acta Phys. Pol. B Proc. Suppl. **163**, 4-A21 (2023)
74. P. Geltenbort and F. Goennenwein, A. Oed, Precision measurements of mean kinetic energy release in thermal-neutron-induced fission of $^{233}$U, $^{235}$U and $^{239}$Pu, in *Conf. on Nucl. Data f. Basic a. Appl. Sci.*, Santa Fe, 985, Vol. 1, p. 393 (1985). https://doi.org/10.1080/00337578608207429
75. K.H. Schmidt, B. Jurado, C. Amouroux et al., General description of fission observables: GEF model code. Nucl. Data Sheets **131**, 107 (2016). https://doi.org/10.1016/j.nds.2015.12.009
76. P. Schillebeeckx, C. Wagemans, A. J. Deruytter et al., Comparative study of the fragments' mass and energy characteristics in the spontaneous fussion of $^{238}$Pu, $^{240}$Pu and $^{242}$Pu and in the thermal-neutron-induced fission of $^{239}$Pu. Nucl. Phys. A **545**, 623 (1992). https://doi.org/10.1016/0375-9474(92)90296-V